

Article

Integrated Control of Motion Actuators for Enhancing Path Following and Yaw Stability of Over-Actuated Autonomous Vehicles

Wenliang Zhang ^{1,*} , Lars Drugge ¹ , Mikael Nybacka ¹  and Jenny Jerrelind ^{1,2} 

¹ Vehicle Dynamics, Department of Engineering Mechanics, KTH Royal Institute of Technology, SE-100 44 Stockholm, Sweden; larsd@kth.se (L.D.); mnybacka@kth.se (M.N.); jennyj@kth.se (J.J.)

² Centre for ECO2 Vehicle Design, KTH Royal Institute of Technology, SE-100 44 Stockholm, Sweden

* Correspondence: wez@kth.se

Abstract: Advanced active safety systems play a crucial role in ensuring the safe driving of vehicles in critical conditions such as an obstacle avoidance manoeuvre. However, conventional techniques relying mainly on braking interventions may not result in the desired vehicle response in such situations. Over-actuation through the control of individual motion actuators could potentially improve the safety performance of vehicles. This study evaluates various configurations of motion actuators for path following and yaw stability control of vehicles in critical driving scenarios. The configurations include active front steering (S), active front steering + torque vectoring (ST), active front steering + active camber (SC) and active front steering + torque vectoring + active camber (STC). The evaluation is achieved based on a nonlinear model predictive control formulation, which considers yaw stability and the physical limits of motion actuators. This problem formulation uses a double-track vehicle model, combined with the Dugoff tyre model and its variant with the camber effect, to model the vehicle dynamics. The actuator configurations are evaluated regarding the passing velocity, tracking accuracy, safety distance and robustness to reference trajectory variation. The results indicate that the integrated control of STC performs the best among all the four configurations while S performs the worst. Furthermore, SC is generally superior to ST.

Keywords: integrated control; yaw stability; path following; over-actuation; nonlinear model predictive control; autonomous vehicle; electric vehicle



Citation: Zhang, W.; Drugge, L.; Nybacka, M.; Jerrelind, J. Integrated Control of Motion Actuators for Enhancing Path Following and Yaw Stability of Over-Actuated Autonomous Vehicles. *Energies* **2023**, *16*, 4776. <https://doi.org/10.3390/en16124776>

Academic Editors: Wiseman Yair and Balázs Németh

Received: 12 April 2023

Revised: 30 May 2023

Accepted: 13 June 2023

Published: 17 June 2023



Copyright: © 2023 by the authors. Licensee MDPI, Basel, Switzerland. This article is an open access article distributed under the terms and conditions of the Creative Commons Attribution (CC BY) license (<https://creativecommons.org/licenses/by/4.0/>).

1. Introduction

Autonomous vehicles (AVs) have been a popular topic in recent years, as they can potentially reduce fatalities and improve efficiency in road transport. At the same time, the driving environment is becoming increasingly complicated, as there exists various road traffic participants, e.g., road vehicles, e-scooter riders, cyclists and pedestrians. Therefore, to ensure the safe driving of vehicles, it is especially important to develop advanced active safety systems, e.g., those for path following and yaw stability control. Although extensive studies, e.g., [1], have been carried out with the aim of achieving yaw stability, purely utilising active steering and/or braking control may not always yield the desired performance. For instance, for the studies conducted in [2–4], the vehicle did not complete the obstacle avoidance manoeuvres with accurate trajectory tracking or without decelerating significantly, leading to compromised safety or comfort for AVs operating in such conditions.

With the introduction of AVs there is a need for by-wire actuation, which has increased the interest in over-actuated vehicle platforms. Here, over-actuation refers to vehicles with more actuators than the degrees of freedom (DoF) to be controlled. For instance, the actuators in a vehicle with individual steering, traction and camber actuation outnumber the DoF to be controlled, i.e., the longitudinal, lateral and yaw directions of the vehicle. This,

compared to conventional vehicles, provides additional DoF for controlling the vehicle, and thus can potentially improve driving safety in addition to other objectives.

Torque vectoring has been studied extensively in order to stabilise the vehicle and/or follow the desired path [5–15]. This is usually achieved by generating a differential yaw moment by individually regulating wheel torques. Specifically, Jonasson et al. [5] explored the capability of torque vectoring for enhancing stability through a safety-critical double-lane change manoeuvre, and showed its potential in improving entry velocity. Nam et al. [6] utilised active front steering and rear-wheel torque vectoring for tracking yaw rate and sideslip angle trajectories, and the lateral stability was improved. Zhai et al. [8] designed torque vectoring algorithms through multi-layer controllers and showed improved lateral stability and manoeuvrability. An adaptive backstepping sliding mode controller was implemented by Zhang et al. [11], which enhanced the vehicle manoeuvrability and stability while being robust to varying vehicle masses and tyre types. Liang et al. [12] controlled an off-road vehicle by exploring torque vectoring and rear-wheel steering, and improved the tracking performance for the yaw rate and sideslip angle. To follow the desired path, an adaptive control scheme was proposed in [13], where the variation in tyre cornering stiffness was considered, with the results showing improved lateral path tracking. Backstepping and model predictive control (MPC) were combined in [14] to follow the given path, and they were found to improve the path tracking and yaw stability. Furthermore, an earlier study by the authors [15] improved path following and yaw stability performances concurrently by exploiting torque vectoring. Although previous studies showed promising findings in applying torque vectoring for improving vehicle stability, the available longitudinal tyre forces and thus the desired yaw moment are limited by the combined slip coupling between longitudinal and lateral tyre forces in such critical driving conditions.

Camber control has also been studied to improve vehicle safety due to its potential to improve lateral tyre forces [16]. For instance, camber control has been utilised to enhance the trajectory tracking performance [17] and to increase the cornering margins [18]. The authors of [19] examined active camber for enhancing the path following and yaw stability performances and found a considerable improvement in the passing velocity and tracking accuracy.

Although existing studies on exploiting over-actuation for achieving active safety have shown promising results, the following points can be further explored. Firstly, there is a lack in comparisons of different over-actuation configurations for AV applications in safety-critical conditions, especially in the context of concurrent path following and yaw stability control. In particular, it is important to evaluate how torque vectoring and active camber can be integrated together to potentially further improve the safety performance. Secondly, previous studies have mainly determined the reference yaw rate and sideslip angle by using single-track models, which is a separate process to path planning. However, this may compromise the overall path following and yaw stability performance. Finally, the robustness of the configuration performance to trajectory variations needs to be explored further.

This study aims to address the issues identified above by evaluating the effect of various over-actuation configurations on the path following and yaw stability performance of AVs in critical driving scenarios. This study mainly contributes to safe autonomous driving in the following three aspects. Firstly, four motion actuator configurations are analysed and compared, i.e., active front steering (S), active front steering + torque vectoring (ST), active front steering + active camber (SC), as well as the integrated control of active front steering + torque vectoring + active camber (STC). The evaluation is achieved through the framework of nonlinear MPC, where constraints on yaw stability and actuator limits are explicitly considered. Secondly, the assessment is carried out based on reference signals obtained through the concurrent yaw rate, sideslip angle and path planning. Finally, an investigation is carried out on the robustness of the over-actuation configurations to reference trajectory variations.

It is important to note that this study does not address the issues of cost and the mechanical system complexity associated with torque vectoring and active camber systems. In fact, there are efforts from the industry devoted to developing these vehicle technologies for electric and autonomous driving applications, e.g., [20,21]. Besides the safety improving advantages as mentioned above, existing studies have already shown the energy saving potential of such vehicle platforms [22,23]. Moreover, these types of vehicle configurations enable various other benefits such as more DoF for vehicle dynamics control [24], fault-tolerance [25] and motion comfort enhancement [26].

2. Vehicle Dynamics Modelling

This section describes the modelling of vehicle movement and tyre forces for four over-actuation configurations, i.e., S, ST, SC and STC. The methods for modelling the vehicle dynamics are detailed in [15,19]. For the sake of completeness, this section presents the modelling of a few key components.

2.1. Vehicle Model

A double-track planar vehicle model (see Figure 1) was used to model the vehicle dynamics used in all four configurations. The model describes the movement of the vehicle in the longitudinal, lateral and yaw directions, and the rotational movement of the four wheels. This model can be represented by the following equations:

$$m\dot{v}_x = -(F_{yfl} + F_{yfr}) \sin \delta_f + (F_{xfl} + F_{xfr}) \cos \delta_f + F_{xrl} + F_{xrr} + mv_y \omega_z \quad (1)$$

$$m\dot{v}_y = (F_{yfl} + F_{yfr}) \cos \delta_f + F_{yrl} + F_{yrr} + (F_{xfl} + F_{xfr}) \sin \delta_f - mv_x \omega_z \quad (2)$$

$$I_z \dot{\omega}_z = l_f (F_{yfl} + F_{yfr}) \cos \delta_f - l_r (F_{yrl} + F_{yrr}) + \frac{B_f}{2} (F_{yfl} - F_{yfr}) \sin \delta_f + \frac{B_f}{2} (F_{xfr} - F_{xfl}) \cos \delta_f + \frac{B_r}{2} (F_{xrr} - F_{xrl}) + l_f (F_{xfl} + F_{xfr}) \sin \delta_f \quad (3)$$

$$\dot{X} = v_x \cos \psi - v_y \sin \psi \quad (4)$$

$$\dot{Y} = v_x \sin \psi + v_y \cos \psi \quad (5)$$

$$\dot{\psi} = \omega_z \quad (6)$$

$$I_{wi} \dot{\omega}_i = T_i - r_e F_{xi} \quad (i \in \mathcal{A}). \quad (7)$$

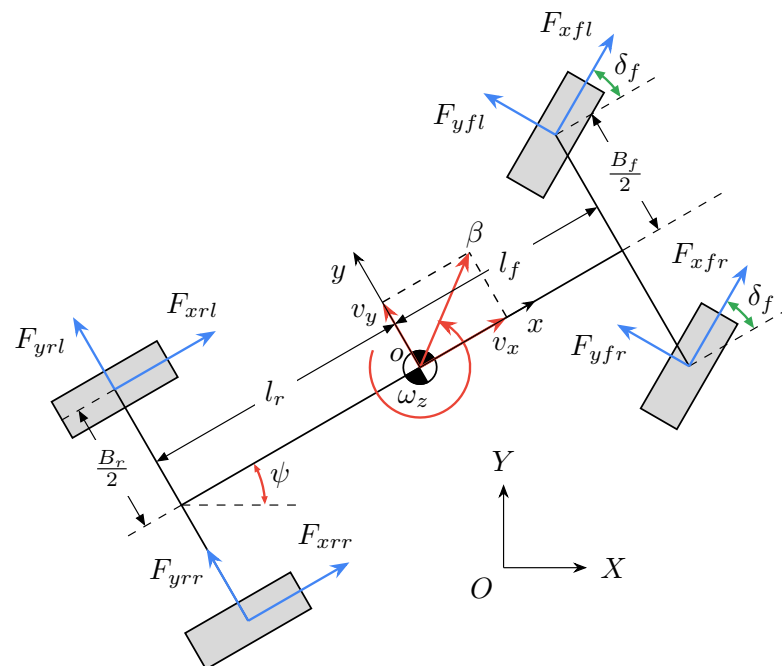


Figure 1. Double-track planar vehicle model [27].

In order to calculate the longitudinal and lateral tyre forces, F_{xi} and F_{yi} ($i \in \mathcal{A}$), the vertical wheel load is determined by considering the load transfer among the four wheels with the steady-state equations from [28]:

$$F_{zfl} = \frac{l_r mg}{2(l_f + l_r)} - \frac{h_g ma_x}{2(l_f + l_r)} - \frac{l_r h_g ma_y}{B_f(l_f + l_r)} \tag{8}$$

$$F_{zfr} = \frac{l_r mg}{2(l_f + l_r)} - \frac{h_g ma_x}{2(l_f + l_r)} + \frac{l_r h_g ma_y}{B_f(l_f + l_r)} \tag{9}$$

$$F_{zrl} = \frac{l_f mg}{2(l_f + l_r)} + \frac{h_g ma_x}{2(l_f + l_r)} - \frac{l_f h_g ma_y}{B_r(l_f + l_r)} \tag{10}$$

$$F_{zrr} = \frac{l_f mg}{2(l_f + l_r)} + \frac{h_g ma_x}{2(l_f + l_r)} + \frac{l_f h_g ma_y}{B_r(l_f + l_r)}. \tag{11}$$

2.2. Tyre Model

As can be seen from Equations (1)–(3), longitudinal and lateral tyre forces are required in the vehicle model equations. Due to its effectiveness and simplicity, the Dugoff tyre model [29] was used to calculate the nonlinear, combined slip tyre forces for the configurations S and ST, with the equations given by

$$F_{xi} = C_{\kappa i} \frac{\kappa_i}{1 + \kappa_i} f(\lambda_i) \tag{12}$$

$$F_{yi} = C_{\alpha i} \frac{\tan \alpha_i}{1 + \kappa_i} f(\lambda_i) \tag{13}$$

$$\lambda_i = \frac{\mu F_{zi}(1 + \kappa_i)}{2((C_{\kappa i} \kappa_i)^2 + (C_{\alpha i} \tan \alpha_i)^2)^{1/2}} \tag{14}$$

$$f(\lambda_i) = \begin{cases} (2 - \lambda_i)\lambda_i, & \text{if } \lambda_i < 1 \\ 1, & \text{if } \lambda_i \geq 1 \end{cases} \tag{15}$$

To utilise camber actuators for path following and yaw stability control, the configurations SC and STC consider the camber effect in tyre modelling. Therefore, besides the Dugoff tyre model denoted by Equation (12), a linear equation (with respect to camber angle) is used to represent the extra lateral tyre force due to wheel camber:

$$F_{y\gamma j} = C_{\gamma j} \gamma_j \tag{16}$$

$$C_{\gamma j} = \begin{cases} C_{\gamma 0j} + C_{\gamma \alpha j} |\alpha_j|, & \text{if } |\alpha_j| < \alpha_{lim} \\ C_{\gamma f j}, & \text{if } |\alpha_j| \geq \alpha_{lim} \end{cases} \tag{17}$$

where $F_{y\gamma j}$ ($j \in \mathcal{B}$) denotes the extra lateral tyre force due to the camber effect at the wheel (left/right); $C_{\gamma j}$ is the camber stiffness; γ_j is the camber angle; $C_{\gamma 0j}$ and $C_{\gamma f j}$ are the camber stiffness when with zero tyre slip angle and when the tyre slip angle, α_j , reaches α_{lim} , respectively, where α_{lim} is a saturation value that depends on the tyre property; and $C_{\gamma \alpha j}$ is the variation in camber stiffness with regard to the tyre slip angle.

Note that the camber stiffness is defined as negative, to be consistent with the definition of cornering stiffness, and the variation in camber stiffness is defined as positive. This means that $|C_{\gamma j}|$ decreases as $|\alpha_j|$ increases until $|\alpha_j|$ reaches α_{lim} , as can be seen in Figure 2. More details regarding camber effect modelling and its influence on lateral tyre forces can be found in [19].

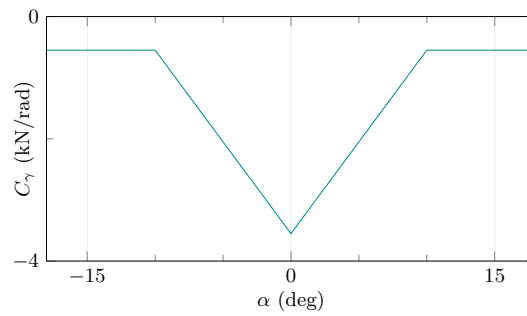


Figure 2. Camber stiffness variation with respect to tyre slip angle.

2.3. Model Summary

Considering the vehicle and tyre modelling described in Sections 2.1 and 2.2, the system state and output vectors, x and y , for controllers S, ST, SC and STC are summarised as

$$x = [v_x \ v_y \ \omega_z \ \psi \ X \ Y \ \omega_{fl} \ \omega_{fr} \ \omega_{rl} \ \omega_{rr}]^T \quad (18)$$

$$y = [\omega_z \ \beta \ \psi \ Y \ v_x]^T, \quad (19)$$

where v_x and v_y are the longitudinal and lateral velocities at the centre of gravity (CoG) of the vehicle; ω_z denotes the vehicle yaw rate at the CoG; ψ is the yaw angle; X and Y represent the longitudinal and lateral positions of the vehicle, respectively; and ω_i ($i \in \mathcal{A}$) denotes the angular velocity of the front left, front right, rear left and rear right wheels, respectively. Additionally, $\beta = \arctan v_y/v_x \approx v_y/v_x$ (valid for a small angle) signifies the vehicle sideslip angle. As can be seen from the figures given in Section 4, the maximum sideslip angle during the tests was around 8° , and the actual sideslip angle should always be smaller than 11° , considering the limits applied to it. A simple calculation shows that $\beta = 11^\circ = 0.192 \text{ rad} \approx \arctan(0.192 \text{ rad}) = 0.190 \text{ rad}$, validating the assumption of a small sideslip angle.

Moreover, considering the fact that different combinations of actuators are utilised in the controllers, the system input vectors, u , for controllers S, ST, SC and STC are defined by Equations (20)–(23), respectively, as follows:

$$u = [\delta_f \ T]^T \quad (20)$$

$$u = [\delta_f \ T_{fl} \ T_{fr} \ T_{rl} \ T_{rr}]^T \quad (21)$$

$$u = [\delta_f \ T \ \gamma_f \ \gamma_r]^T \quad (22)$$

$$u = [\delta_f \ T_{fl} \ T_{fr} \ T_{rl} \ T_{rr} \ \gamma_f \ \gamma_r]^T, \quad (23)$$

where δ_f is the steering angle at the front wheels, T and T_i ($i \in \mathcal{A}$) are the torque at the four wheels, and γ_f and γ_r are the camber angle of the front and rear wheels, respectively.

The four controllers mainly differ in two aspects in terms of modelling. Firstly, they have different levels of actuation capabilities, as can be seen in Equation (20). Specifically, the configuration S cannot exploit torque vectoring, meaning that it would generate the same torque command to all four wheels. This is why, for the configuration S, Equation (7) becomes

$$I_w \dot{\omega} = T - r_e F_x, \quad (24)$$

and, accordingly, merely one variable corresponding to wheel torque is included in Equation (20). Compared with configuration S, ST and SC can exploit torque vectoring and active camber, respectively, and thus Equations (21) and (22) are used for them. As for STC, it integrates the usage of both torque vectoring and active camber for controlling the vehicle. Therefore, (23) is set as the input vector for STC. Secondly, the four configurations

differ in the adoption of tyre models, while S and ST use the Dugoff tyre model given in Equation (12), SC and STC additionally consider camber modelling with Equation (16).

Combining the models described in Equations (1)–(16) and (24), as well as the system variables defined in Equations (18)–(20), results in continuous time system dynamics. With the collocation method as detailed in Section 3.2, the modelling for controllers S, ST, SC and STC can be denoted with the following discrete time form:

$$x_{k+1} = f(x_k, u_k) \quad (25)$$

$$y_k = h(x_k) \quad (26)$$

where the function $h(\cdot)$ denotes a nonlinear relationship between the state and output vectors as given in Equation (18).

3. Controller Design

This section presents the design of the four controllers, i.e., S, ST, SC and STC. The main purposes of these controllers are to follow the reference trajectories given by an upper-level planner while maintaining yaw stability in safety-critical driving conditions. To achieve this, nonlinear MPC is used as the framework for designing the controllers, due to its capability of predicting future vehicle trajectories and due to it explicitly considering constraints in its formulation.

3.1. Formulation

When designing the nonlinear MPC controllers, the tracking errors of the reference trajectories, as well as the magnitude of the control actions and their variation, are included in the cost function. Additionally, constraints on the state and control variables are explicitly considered. The nonlinear MPC [30] is formulated as follows:

$$\begin{aligned} \min_{x, x_c, u, \Delta u, s} & \underbrace{\sum_{p=0}^{N-1} \|y_{k+p|k} - y_{k+p|k}^{ref}\|_{Q_y}^2}_{\text{tracking error}} + \underbrace{\sum_{p=0}^{N-1} \|u_{k+p|k}\|_{R_u}^2}_{\text{control action}} + \underbrace{\sum_{p=0}^{N-1} \|\Delta u_{k+p|k}\|_{R_{du}}^2}_{\text{change of control action}} \\ & + \underbrace{\sum_{p=0}^{N-1} \|s_{k+p|k}\|_{Q_s}^2}_{\text{slack term}} + \underbrace{\|y_{k+N|k} - y_{k+N|k}\|_{Q_{yf}}^2}_{\text{terminal cost of tracking error}} + \underbrace{\|s_{k+N|k}\|_{Q_{sf}}^2}_{\text{terminal cost of slack variable}} \end{aligned} \quad (27)$$

$$\text{s. t. } x_{k+p+1|k} = f(x_{k+p|k}, u_{k+p|k}) \quad y_{k+p|k} = h(x_{k+p|k}), \quad p \in \{0, 1, \dots, N\} \quad (28)$$

$$\Pi(x_k, x_c, k, x_{c,k+p|k,q}) = f_c(x_{c,k+p|k,q}, u_{k+p|k}), \quad q \in \{0, 1, \dots, N_c\} \quad (29)$$

$$\Delta u_{k+p|k} = \begin{cases} u_{k+p|k} - u_{k+p-1|k}, & \text{if } p \geq 1 \\ u_{k|k} - u_{k-1|k-1}, & \text{if } p = 0 \end{cases} \quad (30)$$

$$u_{min} \leq u_{k+p|k} \leq u_{max} \quad \Delta u_{min} \leq \Delta u_{k+p|k} \leq \Delta u_{max} \quad (31)$$

$$g(x_{k+p|k}, s_{k+p|k}) \leq 0 \quad s_{k+p|k} \geq 0 \quad (32)$$

where $x = [x_{k+1|k}, \dots, x_{k+N|k}]$, $u = [u_{k|k}, \dots, u_{k+N-1|k}]$, $\Delta u = [\Delta u_{k|k}, \dots, \Delta u_{k+N-1|k}]$ and $s = [s_{k|k}, \dots, s_{k+N|k}]$ are sequences of vectors for the state, control, variation of control and slack variables over the prediction horizon, N , respectively. $x_c = [x_{c,k|k,1}, \dots, x_{c,k|k,N_c}, \dots, x_{c,k+N-1|k,N_c}]$ denotes a sequence of $N \times N_c$ collocation states over the prediction horizon, where N_c is the number of interior collocation points. Moreover, Δu is an affine function of u , as can be seen in Equation (31).

As can be seen from Equation (27), the cost function consists of six terms of L2-norm. For instance, $\|u_{k+p|k}\|_{R_u}^2$ can be expressed as $u_{k+p|k}^T R_u u_{k+p|k}$. The six terms penalise the trajectory tracking errors and the magnitude of control actions and their variation with the corresponding weight matrices Q_y , R_u , R_{du} , Q_{yf} , Q_s and Q_{sf} , respectively. These matrices

are chosen to be positive definite with merely diagonal elements being non-zero, and their values are set as in Equation (34). Note that the terminal terms are used together with the slack terms as a measure to ensure the stability of the MPC problem, as suggested in [30,31].

The constraints in the nonlinear MPC formulation account for yaw stability (denoted by yaw rate and sideslip angle) and actuator capacity, as defined by Equations (31) and (32). Specifically, the yaw stability constraints can be further expressed as

$$g(x_{k+p|k}, s_{k+p|k}) = \begin{bmatrix} \omega_{zmin} - \omega_{z,k+1|k} - s(1)_{k+p|k} \\ \beta_{min} - \beta_{k+1|k} - s(2)_{k+p|k} \\ \omega_{z,k+1|k} - \omega_{zmax} - s(1)_{k+p|k} \\ \beta_{k+1|k} - \beta_{max} - s(2)_{k+p|k} \end{bmatrix} \leq 0 \quad (33)$$

where the function $g(\cdot)$ relates nonlinearly to the state variables. As can be seen, the non-negative slack vector $s_{k+p|k}$ is imposed on the yaw rate and sideslip angle constraints to avoid possible infeasibility issues when solving the optimisation problem.

Reference trajectories denoting yaw stability, i.e., the reference yaw rate and sideslip angle, are usually calculated by using a single-track model and the actual steering angle, e.g., in [32], and/or determined separately from the reference path and steady-state steering angle, e.g., in [15]. In the present study, an optimisation-based trajectory planner, as developed in [33], is used to concurrently generate reference trajectories, including the reference yaw rate, sideslip angle and path, as well as the yaw rate and sideslip angle constraints. A planner, together with a model-based method, are adopted for trajectory generation because they can naturally handle nonlinearity and constraints in their formulation.

3.2. Implementation

For practical implementation of the nonlinear MPC controllers on digital devices, a discrete time system is often required. To discretise the continuous time system and efficiently handle the corresponding infinite-dimensional optimisation problem, direct optimal control techniques can be adopted. Consequently, the infinite-dimensional optimisation problem can be converted into a finite one, e.g., the nonlinear MPC formulation as given in Equation (27).

The prevailing direct approaches include direct single shooting (DSS) [34], direct multiple shooting (DMS) [35] and direct collocation (DC) [36]. While DSS eliminates state variables from the resulting optimal control problem (OCP), DMS keeps both the state and control variables and treats the corresponding system equations as equality constraints. Compared to DMS, DC further divides each of the discretised sampling intervals into several sub-intervals, and a polynomial is used to associate the containing collocation states. It is obvious to see that, for the same problem, DMS would yield a larger OCP than DSS, as DMS produces more decision variables and constraints. On the other hand, the resulting OCP from DMS is much sparser than DSS, and DC gives an even sparser OCP than DMS. Fortunately, such a sparse structure can be exploited with interior point methods (IPMs), e.g., with the optimisation tool IPOPT [37], and thus the resulting OCP from DC can be solved more efficiently than DMS and DSS.

From Equation (27), it can be seen that the nonlinear MPC forms a complicated optimisation problem, as it involves nonlinearity in the cost function and constraints and consists of various decision variables. Nevertheless, the computational efficiency of the nonlinear MPC can be significantly improved by using the DC method as discussed above. Applications and discussions of these direct approaches on solving nonlinear MPC and moving horizon estimation (MHE) [38,39] problems can be found in [15,27], [19] (Section 3.4) and [40] (Chapter 6).

In the present study, the resulting nonlinear MPCs from the four controllers are designed by using `MPCtools` [41], which is an interface for implementing MPC problems. With this tool, MPC-related configurations can be naturally defined, e.g., state, control and slack variables, cost functions, system equations and state and control constraints. The non-

linear MPC problem defined in `MPCTools` is interpreted by `CasADi` [42] and transferred to IPOPT as an optimisation problem, which is then solved by the solver MA27 [43].

4. Results and Discussion

This section presents an evaluation of four motion actuator combinations through the controllers designed in Section 3, i.e., S, ST, SC and STC. For a fair comparison, the four controllers share the same form of nonlinear MPC formulation as given in Equation (27), are implemented in the same manner and are evaluated in the same framework shown in Figure 3. The main differences between the four controllers are that they have different state equations, control vectors and tuning parameters, as detailed in Equation (34).

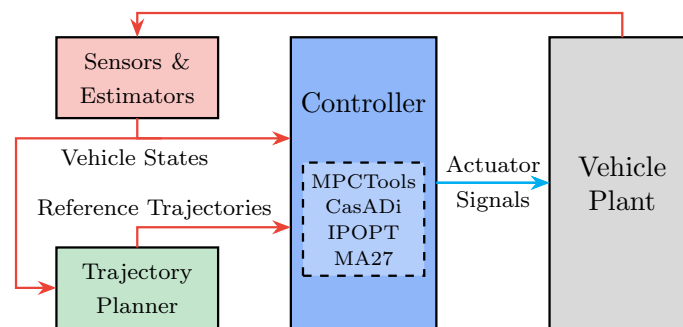


Figure 3. Controller evaluation framework. “Actuator Signals” denotes the control inputs of different controllers.

During the evaluation, a vehicle plant model that features the KTH Research Concept Vehicle (RCV) [44] was used to simulate the vehicle behaviour. Specifically, the vehicle plant has the capability to individually steer, drive/brake and camber each wheel. The plant model was developed in Dymola [45] with the physical modelling language `Modelica` and the Vehicle Dynamics Library. As a result of this, the vehicle plant can be modelled by considering the detailed components of a vehicle, e.g., springs and dampers. As a result, the main components of the plant model include front and rear suspensions, Pacejka tyre models [46], steer, drive and camber actuators and an aerodynamics unit. Additional modelling details, model parameters and an illustration of this Dymola vehicle plant can be found in [15] (Section II-E) and [40] (Figure 2.7). Finally, the Dymola plant model was exported as a functional mock-up unit (FMU) [47] for co-simulation with the nonlinear MPC controllers implemented with `MPCTools`. The FMU vehicle plant contains 44 continuous states and 57,330 variables, making it much more advanced than the controller model denoted by Equation (25). Therefore, this FMU plant model is a suitable choice for comparing the four motion actuation configurations and assessing their robustness.

The results from the four motion actuator configurations are generated with the following two steps:

- Reference trajectories are generated with various initial velocities in a single-lane change (SLC) manoeuvre [33] by using two trajectory planners to test the robustness of the configurations. The advanced trajectory planner is modelled by using a double-track vehicle model that considers load transfer (Planner `DTMlt` in [33]) and the Pacejka tyre model [46]. The simplified planner adopts a single-track vehicle model and a linear tyre model, and it does not include the sideslip angle variation term in the yaw rate constraint as does the advanced planner.
- The four controllers are used to control the vehicle by following the reference trajectories, i.e., the reference yaw rate, sideslip angle, yaw angle, lateral position and longitudinal velocity, while complying with the yaw stability constraints, i.e., the constraints on the yaw rate and sideslip angle, at various initial velocities in the SLC manoeuvre. Both the reference trajectories and the yaw stability constraints directly come from the trajectory planners.

With the results obtained as above, the four over-actuation configurations are evaluated from three aspects as detailed in Sections 4.1–4.3.

- Passing velocity and tracking accuracy. In particular, the highest passing velocity refers to the maximum initial velocity that the vehicle is able to complete the manoeuvre at while not colliding with the lane boundary, and tracking accuracy is quantified by using the performance indicators RMS and maximum tracking error, as detailed in [15] (Section IV).
- Safety distance, i.e., the distance between vehicle corners and the lane boundary at four critical locations.
- Robustness test, i.e., the performance consistency against reference trajectory variations.

As an example, Figure 4 shows the generated reference trajectories from the advanced planner in the SLC manoeuvre with an initial of being 73 km/h. Similarly, reference trajectories are generated at various other initial velocities from both the advanced and simplified planners (results not shown to save space). Subsequently, these reference trajectories are used by the four controllers for trajectory tracking in the following discussions.

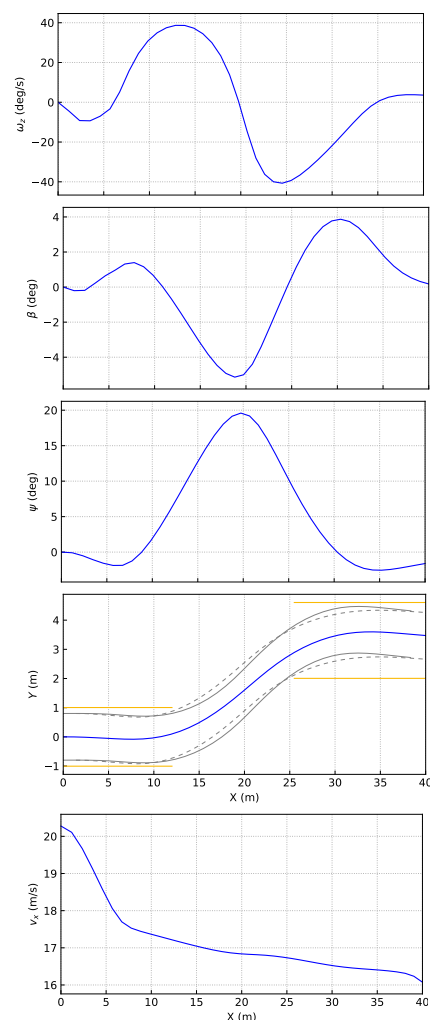


Figure 4. Reference trajectories from the advanced planner in the SLC manoeuvre at the initial velocity of 73 km/h. They show the planned yaw rate (ω_z), sideslip angle (β), yaw angle (ψ), lateral position (Y) and longitudinal velocity (v_x), respectively. The solid yellow lines denote the lane boundary for the SLC track, and the grey lines denote the trajectories of the four vehicle corners, with the dashed lines showing the front corners and the solid lines the rear corners.

Considering their physical limits, the capability of the steering, torque and camber actuators of the vehicle are constrained to be within $\pm 25^\circ$, ± 1490.2 Nm and $\pm 15^\circ$, respectively.

Accordingly, the rates of change of these actuators are defined as $\pm 37^\circ/s$, $\pm 2980.5 \text{ Nm/s}$ and $\pm 45^\circ/s$, respectively.

As different combinations of actuators are considered in the four controllers, the weight matrices are set accordingly for each controller. Specifically, the same components in the weight matrices are used for all the controllers where applicable, for a fair comparison. To this end, the tuning parameters for the four controllers are set as follows:

$$R_{u,s} = R_{du,s} = \text{diag}([10 \ 20 \times 10^{-6}]) \tag{34}$$

$$R_{u,sc} = R_{du,sc} = \text{diag}([10 \ 20 \times 10^{-6} \ 10 \ 10]) \tag{35}$$

$$R_{u,st} = R_{du,st} = \text{diag}([10 \ 5 \times 10^{-6} \ 5 \times 10^{-6} \ 5 \times 10^{-6} \ 5 \times 10^{-6}]) \tag{36}$$

$$R_{u,stc} = R_{du,stc} = \text{diag}([10 \ 5 \times 10^{-6} \ 5 \times 10^{-6} \ 5 \times 10^{-6} \ 5 \times 10^{-6} \ 10 \ 10]) \tag{37}$$

$$Q_{y,s} = Q_{y,st} = Q_{y,sc} = Q_{y,stc} = \text{diag}([120 \ 30 \ 30 \ 100 \ 10]) \tag{38}$$

$$Q_{s,s} = Q_{s,st} = Q_{s,sc} = Q_{s,stc} = \text{diag}([10^6 \ 10^6]) \tag{39}$$

$$Q_{y,f,\cdot} = Q_{y,\cdot} \quad Q_{s,f,\cdot} = Q_{s,\cdot} \quad N = 33 \quad N_c = 1. \tag{40}$$

When tuning the weight matrices, the unit and relative importance of the corresponding variables are considered. For instance, the steering angle (rad) has a considerably larger component than the wheel torque (Nm) in the $R_{u,\cdot}$ matrix, considering that SI (International System of Units) units are adopted. Additionally, $Q_{y,\cdot}$ generally has larger components than $R_{u,\cdot}$, as trajectory tracking is more important than actuator usage in the present study. Moreover, the purpose of using a significantly large $Q_{s,\cdot}$ matrix is to penalise the potential violation of the state constraint, as defined in Equation (33). Finally, a preview time of around 1 s is selected. This then is used to determine the horizon length 33, in the case that the sampling interval from the planner trajectories is around 30 ms. A more detailed description of the tuning process can be found in [15] (Section IV).

4.1. Velocity and Accuracy

Table 1 shows the highest passing velocity of the four configurations with the reference trajectories from the advanced planner. As can be seen, the configuration S yields the lowest passing velocity among all the configurations, which is 3 km/h lower than that from ST and SC; on the other hand, STC has a 6 km/h higher passing velocity than the configuration S.

Table 1. Highest passing velocity of the four motion actuator configurations with trajectories from the advanced planner.

Configuration	S	ST	SC	STC
Velocity (km/h)	73	76	76	79

The configuration S produces in general the largest tracking errors for the yaw rate, sideslip angle and yaw angle at the initial velocity of 73 km/h with the advanced planner, as shown in Table 2 and Figure 5. It can also be seen that ST results in a lower tracking accuracy than SC at the same initial velocity with the advanced planner. On the other hand, at the same initial velocity, STC in general results in smaller tracking errors for the yaw rate, sideslip angle and yaw angle than the other configurations, as can be seen in Table 2 and Figure 5. Moreover, when the initial velocity increases to 76 km/h, STC produces a smaller peak sideslip angle than the other configurations at the position around 20 m, as can be seen in Figure 6b.

Table 2. Trajectory tracking errors of the four motion actuator configurations with reference trajectories from the advanced planner.

v_{xi} (km/h)	Configuration	ω_z ($^{\circ}/s$)		β ($^{\circ}$)		ψ ($^{\circ}$)	
		e_{rms}	e_{max}	e_{rms}	e_{max}	e_{rms}	e_{max}
73	S	3.2	7.7	0.6	1.0	0.9	1.9
	ST	2.9	7.7	0.5	0.9	0.8	1.7
	SC	2.0	6.0	0.3	0.7	0.6	1.5
	STC	2.0	6.9	0.2	0.4	0.5	1.2
76	ST	3.6	11.4	0.6	1.3	0.9	2.1
	SC	2.5	9.2	0.4	1.3	0.6	1.3
	STC	2.6	8.6	0.2	0.6	0.6	1.5
79	STC	3.3	9.6	0.5	1.2	0.8	2.5

The text colour red indicates the largest tracking error (at the same initial velocity) of each column, while the text colour blue indicates the smallest tracking error.

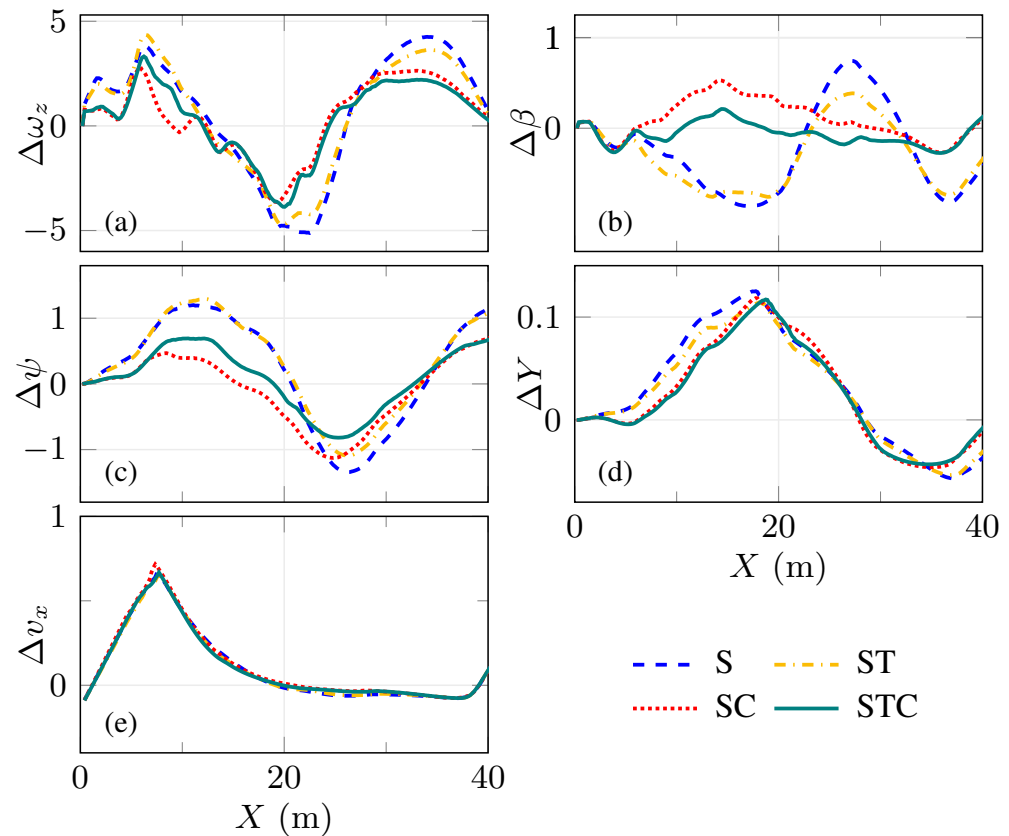


Figure 5. Comparison of trajectory tracking errors of the four motion actuator configurations with the trajectories from the advanced planner at the initial velocity of 73 km/h. (a–e) show the trajectory tracking errors corresponding to the yaw rate (ω_z), sideslip angle (β), yaw angle (ψ), lateral position (Y) and longitudinal velocity (v_x), respectively.

The improved performance of the configuration SC over ST is mainly due to the fact that active camber is more effective than torque vectoring in the present study. Firstly, ST needs to produce an appropriate amount of total longitudinal forces such that it satisfies the longitudinal movement requirement indicated by Equation (1). However, this may limit ST in generating the required yaw moment. Secondly, the capability of torque vectoring is limited by the coupled longitudinal and lateral tyre forces through friction circle/ellipse constraints [46]. Specifically, the vehicle brakes and steers simultaneously at a position of around 10 m (see Figure 6g,k). In such combined slip conditions, relatively large lateral tyre forces are required because the vehicle needs to maintain yaw stability (see Figure 7b,f).

This then indicates that it cannot be realistic to generate larger longitudinal tyre forces from certain wheels for a larger torque vectoring (see Figure 6k). As a result, the build-up of critical vehicle states, e.g., the sideslip angle, from ST is quicker than that from SC, as shown in Figure 6b. In contrast, the improved performance of SC over ST can be attributed to the following two points. Firstly, the lateral tyre forces are much larger than the corresponding longitudinal tyre forces for most of the time in the test scenarios (see Figure 7c,g), meaning that it can be more effective to control the lateral tyre forces than the longitudinal forces. Secondly, with different values of camber angle produced in the front and rear wheels, an additional yaw moment can be generated by controlling the lateral tyre forces, as can be seen from Figures 6h and 7g.

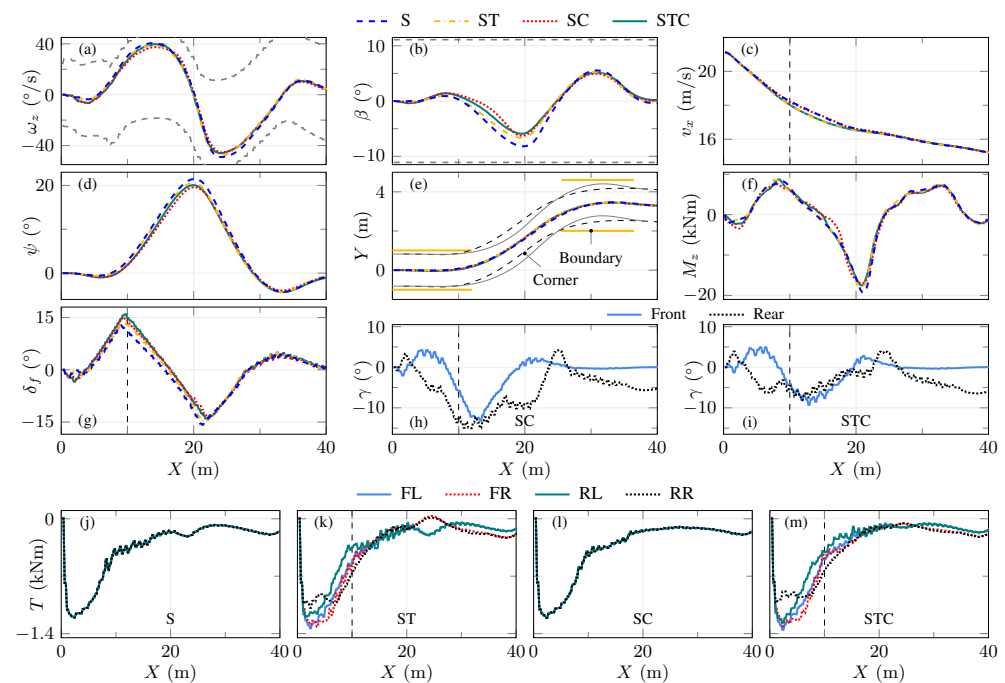


Figure 6. Comparison of trajectory tracking of the four motion actuator configurations with the trajectories from the advanced planner at the initial velocity of 76 km/h. (a–e) show the yaw rate (ω_z), sideslip angle (β), longitudinal velocity (v_x), yaw angle (ψ) and lateral position (Y), respectively, from the vehicle after trajectory tracking. In (f), M_z , which is expressed as the right-hand side of Equation (3), denotes the required yaw moment (from the contribution of both longitudinal and lateral tyre forces) for the yaw movement of the vehicle. (g) presents the commanded front steering angle at the wheel, (h,i) give the commanded camber angle of the front and rear wheels and (j–m) display the commanded drive/braking torques at the wheel. In (a,b), the dashed lines denote the limits for yaw rate and sideslip angle. In (e), “Boundary” denotes the lane boundary for the SLC track, and “Corner” denotes the trajectories of the four vehicle corners corresponding to the configuration S, with the dashed lines showing the front corners and the solid lines showing the rear corners. In (e), it can be seen that the front left corner collides with the lane boundary at around $X = 12$ m.

The working principles of SC can be further explained by examining Figures 6–8. At a position of around $X = 10$ m, the steering angle of the front wheels reaches 13.9° , as shown in Figure 6g, and the tyre slip angles of the four wheels are $\alpha_{fl} = -10.2^\circ$, $\alpha_{fr} = -11.4^\circ$, $\alpha_{rl} = -2.6^\circ$ and $\alpha_{rr} = -2.0^\circ$, respectively, as shown in Figure 8g. This means that, at this position, controlling the inclination angle of the two front wheels may not be as effective as controlling the two rear wheels, considering the relationship between camber stiffness and slip angle, as illustrated in Figure 2. This is why SC produces a camber angle for the rear wheels (-12.2°) twice the value of the front wheels (-5.8°) at this position, as can be seen in Figure 6h. Moreover, the fact that the vehicle is decelerating while steering to the left at this position means the rear right wheel has a larger vertical load than the rear left

wheel, as shown in Figures 6c,g and 8j,k. This explains the higher tyre utilisation in the rear right wheel of SC than that of ST at the position around $X = 10$ m, as can be observed in Figure 8b,c.

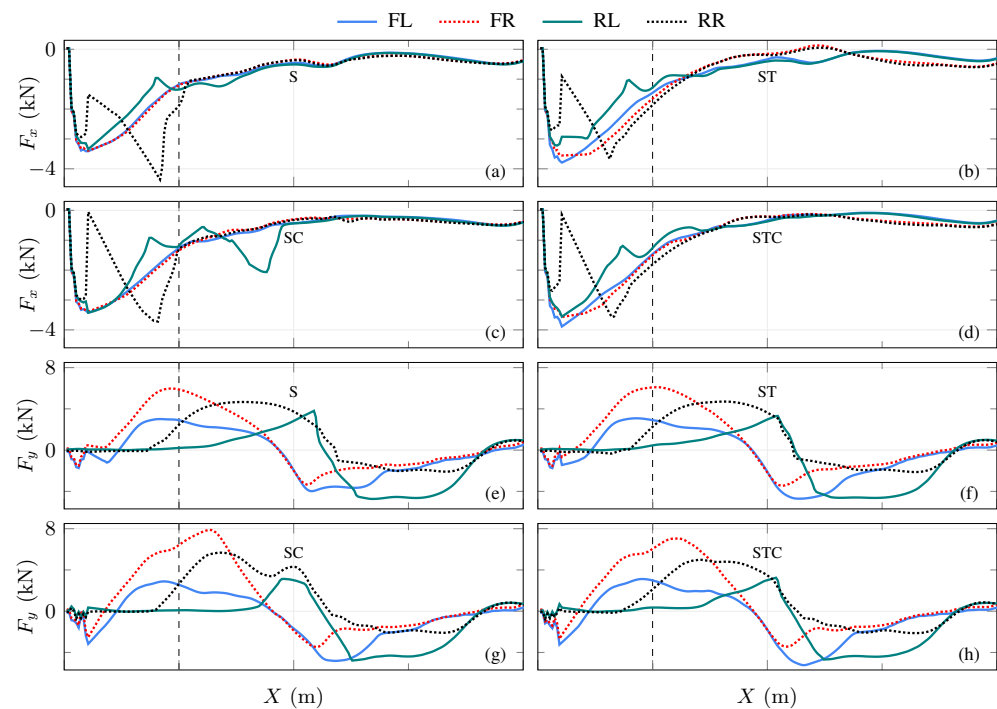


Figure 7. Longitudinal (F_x) and lateral (F_y) tyre forces of the four motion actuator configurations with the trajectories from the advanced planner at the initial velocity of 76 km/h. (a,e), (b,f), (c,g) and (d,h) show the results obtained from S, ST, SC and STC, respectively. It should be noted that, for the configuration S, the vehicle fails to pass the manoeuvre, as explained in Figure 6.

As for the STC configuration, it combines the features of both ST and SC. Therefore, STC does not need to exploit as much torque vectoring as ST to rotate the vehicle at the position around $X = 10$ m, as shown in Figure 6k,m. Moreover, compared with SC, STC results in lower build-up and rate of change in sideslip angle, as well as smaller peak camber demand in the entire manoeuvre, as evident in Figure 6b,h,i. In short, by exploiting the steering, torque and camber actuators in an integrated manner, STC can regulate both the longitudinal and lateral forces of individual wheels when needed, thus resulting in a larger safety margin and an improved performance.

4.2. Safety Distance

Although from Figure 6e it can be seen that the configuration S yields a rather smooth path through the SLC manoeuvre at the initial velocity of 76 km/h, the front left corner of the vehicle in fact collides with the lane boundary at the position around $X = 12$ m. Therefore, this section discusses the safety distance between the four vehicle corners and the lane boundary at four critical locations with the advanced planner. Moreover, safety distance can be viewed as a performance indicator for position tracking, which complements the trajectory tracking results given in Table 2.

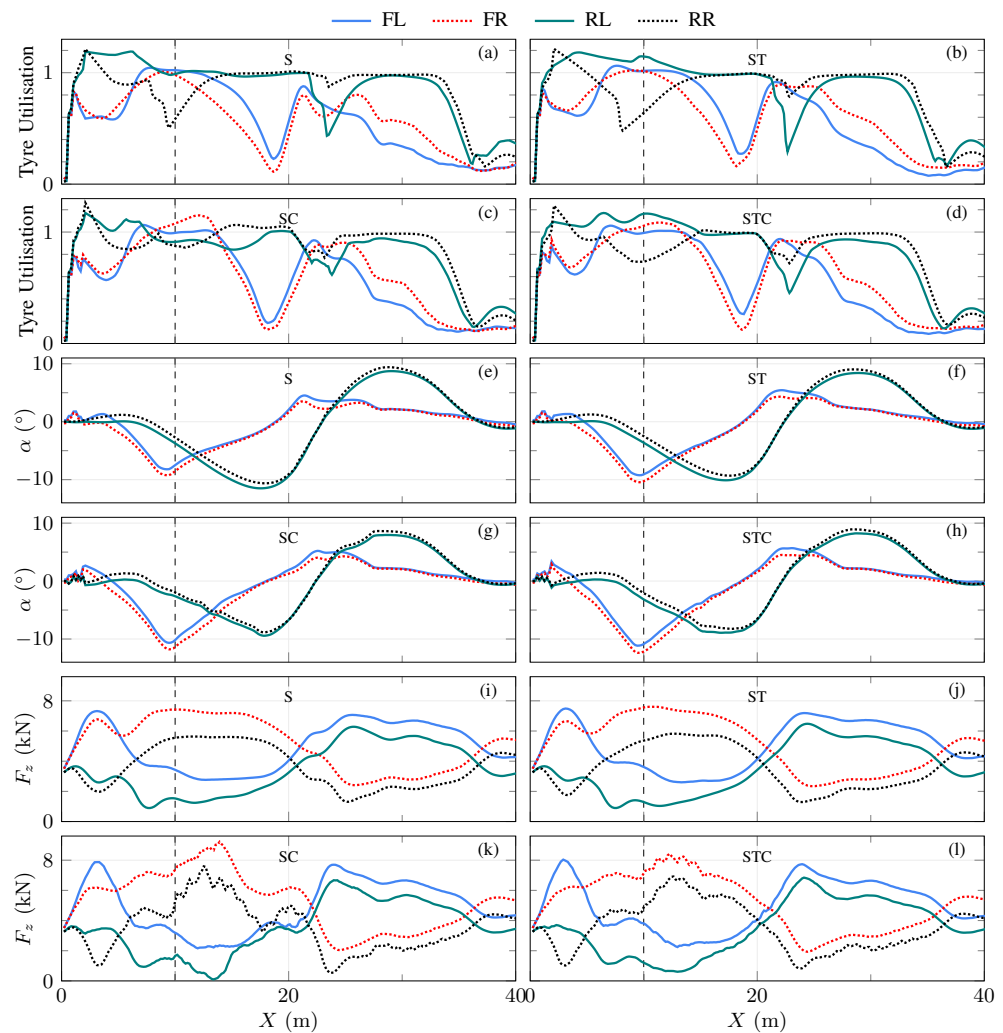


Figure 8. Tyre utilisation, slip angle (α) and vertical load (F_z) of the four motion actuator configurations with the trajectories from the advanced planner at the initial velocity of 76 km/h. (a,e,i), (b,f,j), (c,g,k) and (d,h,l) show the results obtained from S, ST, SC and STC, respectively. The tyre utilisation is calculated by dividing the combined longitudinal and lateral tyre forces with the vertical wheel load and is detailed in [19]. It should be noted that, for the configuration S, the vehicle fails to pass the manoeuvre, as explained in Figure 6.

To identify the critical locations where the vehicle is likely to collide with the lane boundary, tests were carried out for the four controllers at various velocities until the highest passing velocity. The resulted position envelope at the three highest passing velocities (see Table 1) is shown in Figure 9a–c, to make the plots easier to interpret. As can be seen, the vehicle tends to collide with the lane boundary at four positions, which are indicated by “PA”, “PB”, “PC” and “PD”, respectively.

As shown in Table 3, at locations “PA”, “PB”, “PC” and “PD”, the vehicle tends to collide with the lane boundary with the front right, front left, front right and rear left corners, respectively. In general, the vehicle is most likely to collide with the lane boundary at location “PB” for all the configurations. Moreover, at this location, the safety distance from STC increases by 33% (3 cm), compared with that from S and ST, when tested at an initial velocity of 73 km/h. Furthermore, when the velocity increases to 76 km/h, the safety distance (at “PB”) from STC is 166% (5 cm) larger than that from ST. It should be noted that this 5 cm increase in safety distance can be of significant importance in a near crash scenario.

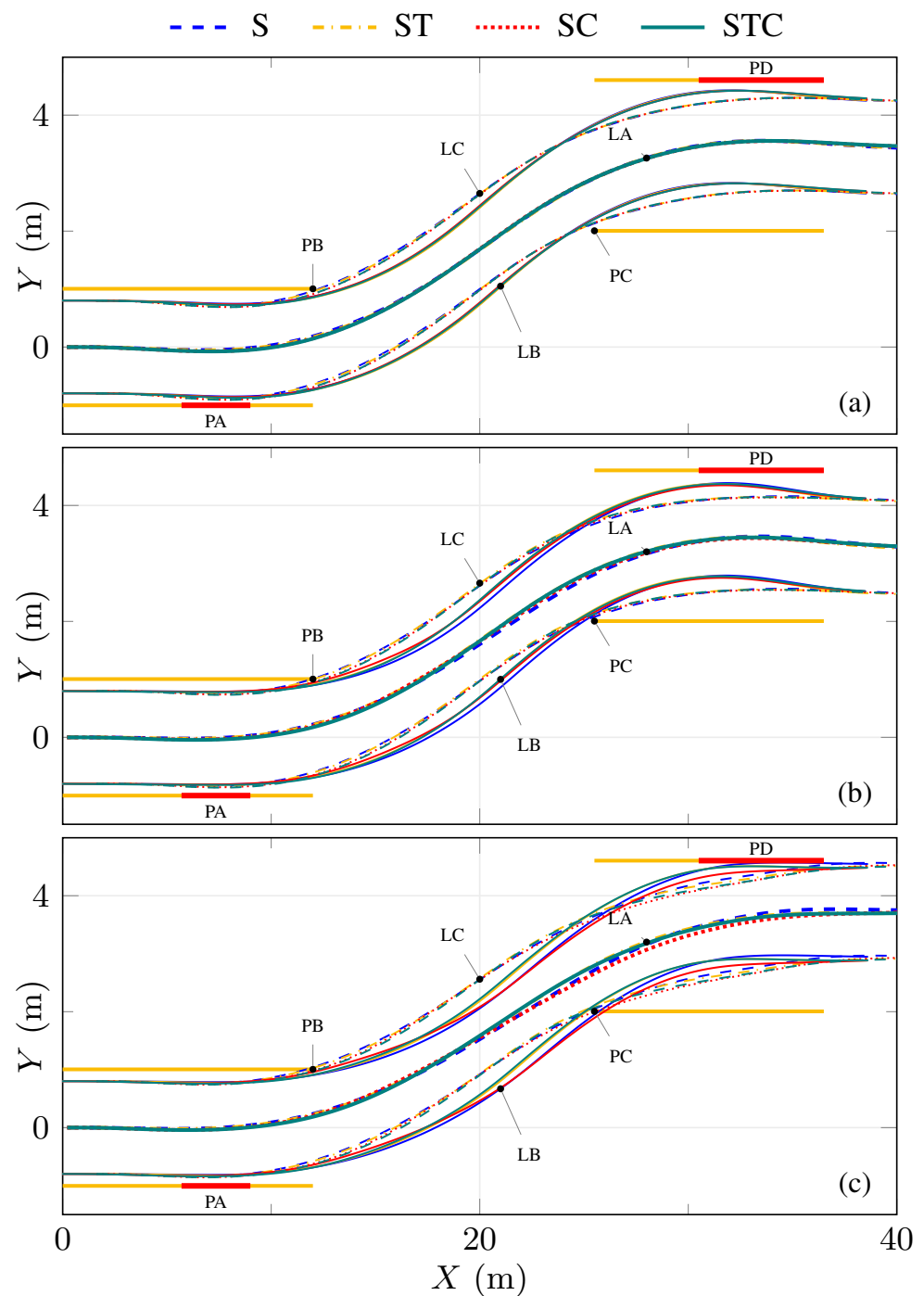


Figure 9. Position envelope of the four motion actuator configurations with trajectories from the advanced planner. (a–c) show the results with the initial velocities of 73, 76 and 79 km/h, respectively. “PA”, “PB”, “PC” and “PD” denote four critical positions where the vehicle tends to collide with the lane boundary. “LA” denotes the position of vehicle centre of gravity with the legend entries shown above this figure. “LB” and “LC” denote the trajectories of the left and right corners of the vehicle, respectively, where the colours indicate the configurations as defined in the legend entries above this figure.

Table 3. Safety distance of the four motion actuator configurations at four critical locations with trajectories from the advanced planner (m).

v_x (km/h)	Configuration	PA (FR)		PB (FL)		PC (FR)		PD (RL)	
		min	X	min	X	min	X	min	X
73	S	0.12	7.6	0.09	11.9	0.14	25.5	0.18	32.1
	ST	0.12	7.6	0.09	12.1	0.14	25.5	0.18	32.1
	SC	0.10	7.8	0.11	12.0	0.15	25.5	0.18	32.4
	STC	0.09	8.0	0.12	11.9	0.15	25.5	0.18	32.4
76	ST	0.17	7.3	0.03	12.0	0.13	25.5	0.23	31.4
	SC	0.14	7.5	0.06	12.0	0.10	25.5	0.26	31.6
	STC	0.14	7.5	0.08	12.0	0.12	25.5	0.23	31.6
79	STC	0.15	6.7	0.04	12.0	0.10	25.4	0.10	33.0

The background colour green indicates the largest safety distance (at the same initial velocity) of each column, while the background colour yellow the shortest safety distance. X indicates the longitudinal position of the vehicle corner where there is the shortest safety distance with respect to the corresponding critical location, e.g., “PB”.

The increased safety distance of STC over ST at “PB” can be explained after examining their location envelopes formed from the four critical locations, e.g., with the initial velocity of 73 km/h. As indicated by Table 3, the resulting overall position envelope (especially the first half of the manoeuvre) from STC shifts closer to the lane boundary on the right side of the vehicle, compared with that from ST. By using this strategy, STC succeeds in manoeuvring the vehicle further away from the lane boundary at the most critical location “PB” and at a higher velocity.

When the initial velocity increases from 73 to 79 km/h, the safety distances of STC at locations “PA”, “PB”, “PC” and “PD” change by 6, −8, −5 and −8 cm, respectively, as shown in Table 3. Taking the right-side corners of the vehicle as an example, this means that the position envelope at “PA” moves to the left while at “PC” it moves to the right. Similarly, it can be seen that the position envelope at “PA” moves backwards along the X axis while at “PD”, it shifts forwards. This means that the envelope tube formed from the trajectories of the vehicle corners is somewhat stretched along the X direction. In other words, when the initial velocity increases, STC tends to produce a smoother position envelope.

4.3. Robustness Test

To assess the robustness of the over-actuation configurations, tests were carried out by using reference trajectories from the simplified planner. As can be seen from Table 4, compared with the configuration S, ST does not gain in passing velocity with the simplified planner, which is worse than the case with the advanced planner, where there was a 3 km/h gain. On the other hand, the passing velocity difference between SC and ST increases from 0 in the case with the advanced planner to 10 km/h with the simplified planner. Moreover, the passing velocity difference between STC and SC with the simplified planner is 2 km/h, which is similar to the case with the advanced planner. Furthermore, the passing velocity gap between STC and S increases to 12 km/h when using the reference trajectories from the simplified planner; in contrast, the passing velocity difference between these two configurations is merely 6 km/h with the advanced planner.

Table 4. Highest passing velocity of the four motion actuator configurations with trajectories from the simplified planner.

Configuration	S	ST	SC	STC
Velocity (km/h)	67	67	77	79

Table 5 and Figures 10 and 11 show the tracking performance of the four configurations with the simplified planner. As can be seen, the configuration S performs the worst

among all the four configurations in terms of the tracking accuracy and the magnitude of the resulting critical vehicle states, e.g., sideslip angle, which is similar to the case with the advanced planner. Moreover, ST again is inferior to SC with the simplified planner with respect to the tracking accuracy and the resulting peak sideslip angle.

Table 5. Trajectory tracking errors of four motion actuator configurations with reference trajectories from the simplified planner.

v_{xi} (km/h)	Configuration	ω_z ($^{\circ}/s$)		β ($^{\circ}$)		ψ ($^{\circ}$)	
		e_{rms}	e_{max}	e_{rms}	e_{max}	e_{rms}	e_{max}
67	S	4.0	9.3	0.7	1.8	1.1	2.2
	ST	3.3	8.3	0.5	1.3	0.9	1.8
	SC	2.1	5.2	0.3	0.6	0.6	1.4
	STC	2.0	5.4	0.3	0.7	0.5	1.2
77	SC	3.3	11.7	0.5	1.2	0.6	1.7
	STC	3.0	10.5	0.4	0.9	0.6	1.5
79	STC	4.0	12.0	0.6	1.6	0.8	1.8

The text colour red indicates the largest tracking error (at the same initial velocity) of each column, while the text colour blue indicates the smallest tracking error.

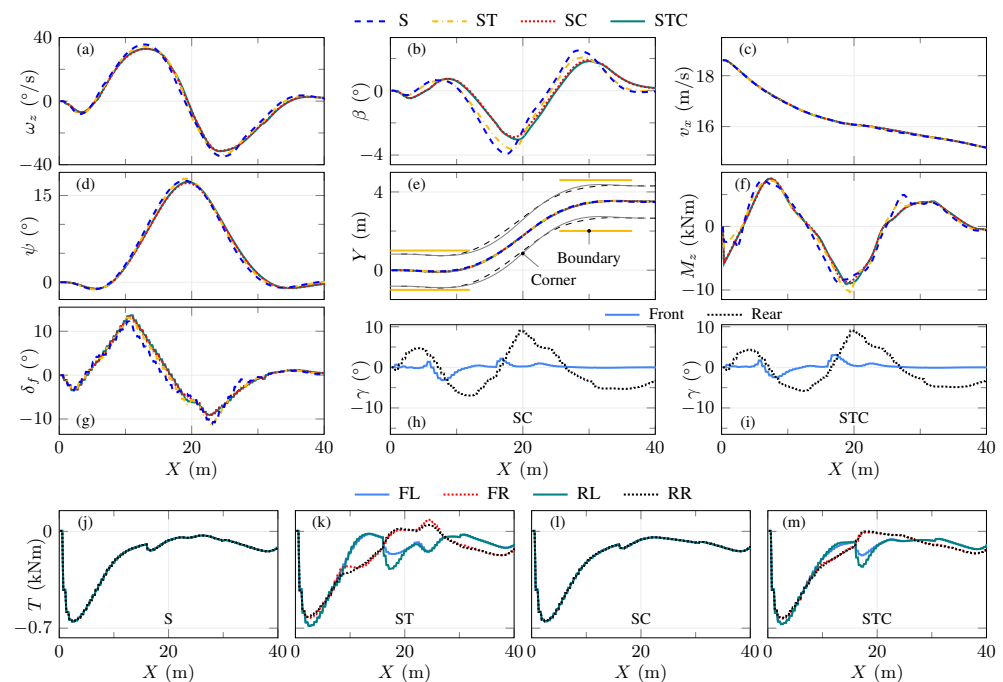


Figure 10. Comparison of trajectory tracking of the four motion actuator configurations with the trajectories from the simplified planner at the initial velocity of 67 km/h. The annotations for the sub-figures can be found in Figure 6.

STC yields a similar tracking accuracy to SC with the simplified planner at the initial velocity of 67 km/h, as can be seen from Table 5 and Figures 10 and 11. This could be due to the fact that, at this relatively low velocity, STC does not need to utilise the full potential of the available actuators. When the initial velocity increases to 77 km/h, STC yields a higher accuracy than SC, as shown in Table 5. Moreover, at this higher velocity, both SC and STC request more actuator usage than the case at 67 km/h, which can be observed in Figure 12a,b, as a result of the more severe driving conditions. Still, at 77 km/h, the peak

camber angle in both the front and rear wheels from STC is lower than that from SC due to its integrated usage of camber and torque actuators.

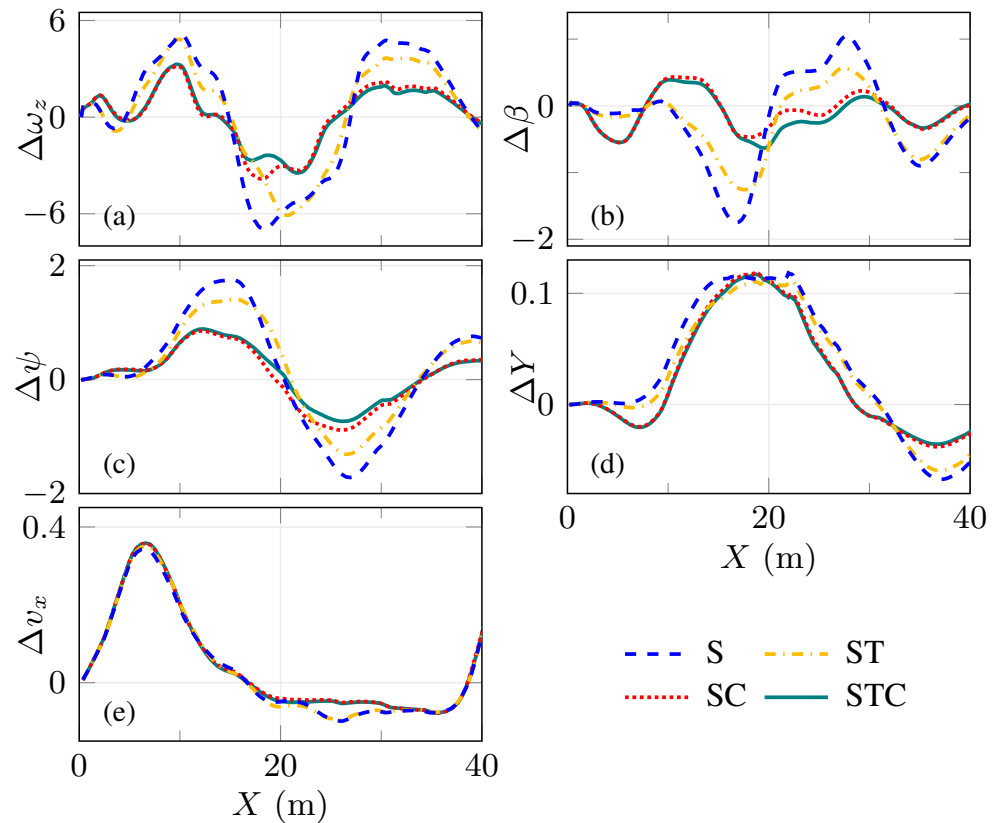


Figure 11. Comparison of trajectory tracking errors of the four motion actuator configurations with the trajectories from the simplified planner and the initial velocity of 67 km/h. The annotations for the sub-figures can be found in Figure 5.

The safety distance of the four configurations at the four critical positions with the simplified planner can be seen in Table 6. “PB” is again the most critical position where the vehicle is likely to collide with the lane boundary for all the configurations. Moreover, the safety distance from STC is 75% larger (3 cm) than that from SC at this location with the initial velocity of 77 km/h. Furthermore, when the initial velocity increases from 67 to 79 km/h, STC also generates a smoother position envelope (the figure for 79 km/h is not shown to save space), which is similar to the observation with the advanced planner.

Table 6. Safety distance of the four motion actuator configurations at four critical locations with trajectories from the simplified planner (m).

v_x (km/h)	Configuration	PA (FR)		PB (FL)		PC (FR)		PD (RL)	
		min	X	min	X	min	X	min	X
67	S	0.12	7.5	0.08	11.9	0.21	25.5	0.25	31.7
	ST	0.12	7.7	0.09	11.9	0.21	25.5	0.25	32.0
	SC	0.10	8.1	0.10	11.9	0.19	25.5	0.24	32.7
	STC	0.10	8.1	0.10	11.9	0.20	25.5	0.23	32.8
77	SC	0.14	7.0	0.04	12.0	0.12	25.5	0.08	33.7
	STC	0.13	7.2	0.07	11.9	0.14	25.6	0.07	33.7
79	STC	0.15	6.7	0.02	12.0	0.14	25.5	0.07	33.0

The background colour green indicates the largest safety distance (at the same initial velocity) of each column, while the background colour yellow the shortest safety distance. X indicates the longitudinal position of the vehicle corner where there is the shortest safety distance with respect to the corresponding critical location.

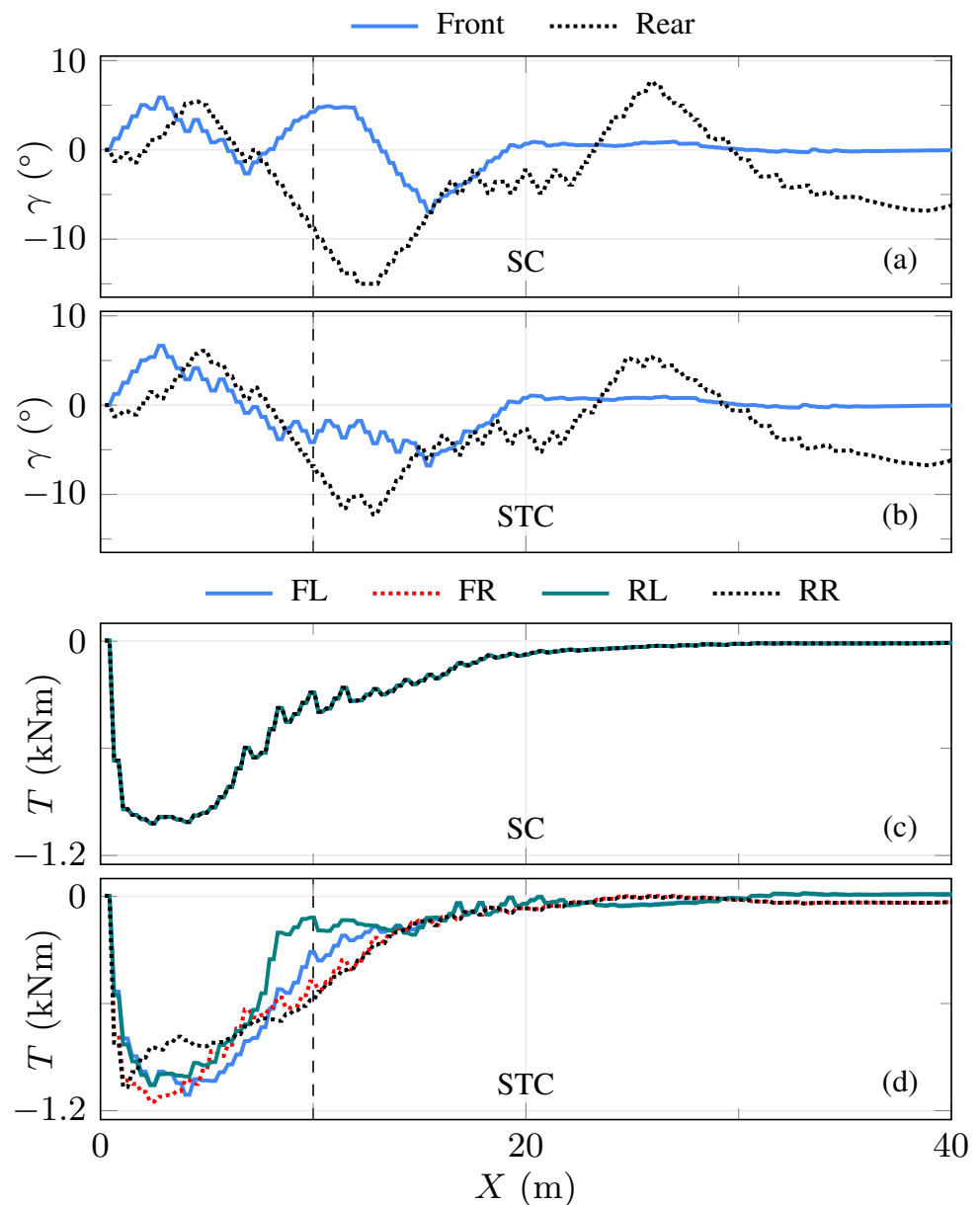


Figure 12. Comparison of control actions of the motion actuator configurations SC and STC with the trajectories from the simplified planner and the initial velocity of 77 km/h. (a,b) show the commanded camber angles at the front and rear axles, and (c,d) display the commanded drive/braking torques at the wheel.

5. Conclusions

This paper has presented an evaluation of four motion actuator configurations for path following and yaw stability control of vehicles in critical driving scenarios. This is achieved through the design of four controllers, i.e., active front steering (S), active front steering + torque vectoring (ST), active front steering + active camber (SC) and active front steering + torque vectoring + active camber (STC). The controllers were designed by using a double-track vehicle model, coupled with the Dugoff tyre model and its variant that includes camber effect. Based on these vehicles and tyre models, the controllers were formulated in the nonlinear MPC framework with considered constraints related to the yaw stability and actuator limits. The four motion actuator configurations were evaluated in the SLC manoeuvre at various initial velocities, with respect to the passing velocity, the tracking accuracy, the safety distance, and the robustness to trajectory generation. The main

findings regarding the performance of these over-actuation combinations are summarised as follows:

- The integrated control of STC yielded the highest passing velocity, i.e., 79 km/h, among all the over-actuation configurations with the reference trajectories from both the advanced and simplified planners. In general, this configuration produced consistently smaller peak values and tracking errors for critical vehicle states, e.g., sideslip angle, than the other configurations with these two types of reference trajectories. Moreover, this configuration generated, in general, a larger safety distance in the most critical position “PB” than the other configurations, which is crucial in near-crash scenarios.
- SC was in general superior to ST in terms of passing velocity, tracking accuracy and safety distance at location “PB” with the two types of reference trajectories, indicating that active camber was more effective than torque vectoring in the tested scenarios.
- S performed in general the worst among all the motion actuator combinations, due to its lack of access to over-actuation.
- S and ST gained 6 and 9 km/h, respectively, in passing velocity when tested with the advanced planner compared to the case with the simplified planner. On the other hand, the passing velocity gap between S and the integrated control of STC increased from 6 km/h with the advanced planner to 12 km/h with the simplified planner. This, in the presented test scenarios, indicates that a simpler motion actuator configuration could benefit more from accurate reference trajectories and that a more advanced configuration could, to a certain degree, compensate for the deficiencies caused by the less accurate trajectories.

In the future, we plan to evaluate the actuator configurations in an experimental vehicle. The influence of more robustness factors on their performance will also be investigated, e.g., modelling uncertainties and estimation errors of key states and parameters [48–50].

Author Contributions: Conceptualisation, W.Z., L.D. and M.N.; software, W.Z.; formal analysis, W.Z., L.D., M.N. and J.J.; writing—original draft preparation, W.Z.; writing—review and editing, W.Z., L.D., M.N. and J.J.; supervision, L.D., M.N. and J.J. All authors have read and agreed to the published version of the manuscript.

Funding: This research was funded by TRENop (Transport Research Environment with Novel Perspectives) at KTH Royal Institute of Technology.

Data Availability Statement: Not applicable.

Conflicts of Interest: The authors declare no conflict of interest.

Abbreviations

The following abbreviations are used in this manuscript:

\mathcal{A}	A set in which the elements denote the front left, front right, rear left and rear right wheels, = $\{fl, fr, rl, rr\}$.
\mathcal{B}	A set in which the elements denote the front and rear (left/right) wheels, = $\{f, r\}$.
XOY	Earth frame; for describing vehicle position.
xoy	Vehicle frame; for describing vehicle motion.
$f(\cdot), h(\cdot)$	Discrete time state, output equation.
$\Pi(\cdot)$	Collocation polynomial equation.
Model Variables	
x, u, y	State, input, output vector.
v_x, v_y	Longitudinal, lateral velocity at centre of gravity (CoG) in frame xoy (m/s).
ω_z	Yaw rate around CoG in frame xoy (rad/s).
ψ	Yaw angle in frame XOY (rad).

X, Y	Longitudinal, lateral position in frame XOY (m).
ω_i	Angular velocity of the wheel (rad/s) ($i \in \mathcal{A}$).
ω	Angular velocity of one wheel (rad/s).
β	Sideslip angle (rad).
a_x, a_y	Longitudinal, lateral acceleration in frame $x_b o y_b$ (m/s^2).
α_i	Tyre slip angle (rad) ($i \in \mathcal{A}$).
κ_i	Tyre slip ratio ($i \in \mathcal{A}$).
δ_f	Steering angle, mean of two front wheels in frame xoy (rad).
γ_f, γ_r	Front, rear camber angle in frame xoy (rad).
T_i	Drive/braking torque on the wheel ($\text{N} \cdot \text{m}$) ($i \in \mathcal{A}$).
T	Drive/braking torque on one wheel ($\text{N} \cdot \text{m}$).
F_{xi}, F_{yi}	Longitudinal, lateral tyre force (N) ($i \in \mathcal{A}$).
F_x	Longitudinal tyre force at one wheel (N).
F_{zi}	Vertical tyre force (N) ($i \in \mathcal{A}$).
Model Parameters	
$C_{\alpha i}$	Tyre cornering stiffness (N/rad) ($i \in \mathcal{A}$).
C_{xi}	Tyre longitudinal stiffness (N) ($i \in \mathcal{A}$).
$C_{\gamma j}$	Tyre camber stiffness (N/rad) ($j \in \mathcal{B}$).
$C_{\gamma 0 j}$	Tyre camber stiffness when with zero slip angle (N/rad) ($j \in \mathcal{B}$).
$C_{\gamma f j}$	Tyre camber stiffness when slip angle reaches α_{lim} (N/rad) ($j \in \mathcal{B}$).
$C_{\gamma \alpha j}$	Variation in camber stiffness with respect to slip angle (N/rad^2) ($j \in \mathcal{B}$).
α_{lim}	Limiting value (depending on tyre property) for determining tyre camber stiffness (rad).
I_{wi}	Wheel rotational inertia ($\text{kg} \cdot \text{m}^2$) ($i \in \mathcal{A}$).
I_w	Rotational inertia of one wheel ($\text{kg} \cdot \text{m}^2$).
r_e	Tyre effective rolling radius (m).
m	Vehicle mass (kg).
I_z	Vehicle yaw inertia ($\text{kg} \cdot \text{m}^2$).
B_f, B_r	Front, rear track width (m).
l_f, l_r	Distance from CoG to front, rear axle (m).
h_g	Height of CoG (m).
μ	Road friction coefficient.
g	Gravitational acceleration (m/s^2).
Controller Variables	
$s_{(\cdot)}$	Slack vector.
x, x_c	Sequence of states, collocation states.
$u, \Delta u, s$	Sequence of vectors for control actions, change of control actions, slack variables.
Controller Parameters	
N	Prediction horizon.
N_c	Number of interior collocation points.
Q_y, Q_{yf}	Weight matrix for penalising stage, terminal output tracking.
$R_u, R_{\Delta u}$	Weight matrix for penalising control and change of control.
Q_s, Q_{sf}	Weight matrix for penalising stage, terminal slack.
u_{min}, u_{max}	Lower, upper boundary on control vector.
$\Delta u_{min}, \Delta u_{max}$	Lower, upper boundary on variation of control vector.
β_{min}, β_{max}	Lower, upper boundary on sideslip angle.
$\omega_{zmin}, \omega_{zmax}$	Lower, upper boundary on yaw rate.

References

1. Liebemann, E.K.; Meder, K.; Schuh, J.; Nenninger, G. *Safety and Performance Enhancement: The Bosch Electronic Stability Control (ESP)*; Technical Paper 2004-21-0060; SAE International: Warrendale, PA, USA, 2004; pp. 421–428.
2. Falcone, P.; Borrelli, F.; Asgari, J.; Tseng, H.E.; Hrovat, D. Predictive Active Steering Control for Autonomous Vehicle Systems. *IEEE Trans. Control Syst. Technol.* **2007**, *15*, 566–580. [[CrossRef](#)]
3. Tjonnas, J.; Johansen, T.A. Stabilization of Automotive Vehicles Using Active Steering and Adaptive Brake Control Allocation. *IEEE Trans. Control Syst. Technol.* **2010**, *18*, 545–558. [[CrossRef](#)]
4. Lee, J.; Choi, S.B. Integrated Control of Steering and Braking for Path Tracking using Multi-Point Linearized MPC. *IEEE Trans. Intell. Veh.* **2022**, *8*, 3324–3335. [[CrossRef](#)]
5. Jonasson, M.; Andreasson, J.; Solyom, S.; Jacobson, B.; Trigell, A.S. Utilization of Actuators to Improve Vehicle Stability at the Limit: From Hydraulic Brakes Toward Electric Propulsion. *J. Dyn. Syst. Meas. Control* **2011**, *133*, 051003. [[CrossRef](#)]

6. Nam, K.; Fujimoto, H.; Hori, Y. Lateral Stability Control of In-Wheel-Motor-Driven Electric Vehicles Based on Sideslip Angle Estimation Using Lateral Tire Force Sensors. *IEEE Trans. Veh. Technol.* **2012**, *61*, 1972–1985.
7. Novellis, L.D.; Sorniotti, A.; Gruber, P.; Orus, J.; Fortun, J.M.R.; Theunissen, J.; Smet, J.D. Direct yaw moment control actuated through electric drivetrains and friction brakes: Theoretical design and experimental assessment. *Mechatronics* **2015**, *26*, 1–15. [[CrossRef](#)]
8. Zhai, L.; Sun, T.; Wang, J. Electronic Stability Control Based on Motor Driving and Braking Torque Distribution for a Four In-Wheel Motor Drive Electric Vehicle. *IEEE Trans. Veh. Technol.* **2016**, *65*, 4726–4739. [[CrossRef](#)]
9. Chatzikomis, C.; Sorniotti, A.; Gruber, P.; Zanchetta, M.; Willans, D.; Balcombe, B. Comparison of Path Tracking and Torque-Vectoring Controllers for Autonomous Electric Vehicles. *IEEE Trans. Intell. Veh.* **2018**, *3*, 559–570. [[CrossRef](#)]
10. Li, B.; Ahmadi, J.; Lin, C.; Siampis, E.; Longo, S.; Velenis, E. Integrated Path-tracking and Control Allocation Controller for Autonomous Electric Vehicle under Limit Handling Condition. In Proceedings of the 2020 IEEE Intelligent Vehicles Symposium (IV), Las Vegas, NV, USA, 19 October 2020–13 November 2020. [[CrossRef](#)]
11. Zhang, L.; Ding, H.; Shi, J.; Huang, Y.; Chen, H.; Guo, K.; Li, Q. An Adaptive Backstepping Sliding Mode Controller to Improve Vehicle Maneuverability and Stability via Torque Vectoring Control. *IEEE Trans. Veh. Technol.* **2020**, *69*, 2598–2612. [[CrossRef](#)]
12. Liang, Z.; Zhao, J.; Dong, Z.; Wang, Y.; Ding, Z. Torque Vectoring and Rear-Wheel-Steering Control for Vehicle’s Uncertain Slips on Soft and Slope Terrain Using Sliding Mode Algorithm. *IEEE Trans. Veh. Technol.* **2020**, *69*, 3805–3815. [[CrossRef](#)]
13. Zhang, Y.; Wang, W.; Wang, W.; Yang, C.; Zhang, Y. An Adaptive Constrained Path Following Control Scheme for Autonomous Electric Vehicles. *IEEE Trans. Veh. Technol.* **2022**, *71*, 3569–3578. [[CrossRef](#)]
14. Wang, C.; He, R.; Jing, Z.; Chen, S. Coordinated Path Following Control of 4WID-EV Based on Backstepping and Model Predictive Control. *Energies* **2022**, *15*, 5728. [[CrossRef](#)]
15. Zhang, W.; Wang, Z.; Drugge, L.; Nybacka, M. Evaluating Model Predictive Path Following and Yaw Stability Controllers for Over-Actuated Autonomous Electric Vehicles. *IEEE Trans. Veh. Technol.* **2020**, *69*, 12807–12821. [[CrossRef](#)]
16. Ammon, D. Vehicle dynamics analysis tasks and related tyre simulation challenges. *Veh. Syst. Dyn.* **2005**, *43*, 30–47. [[CrossRef](#)]
17. Gáspár, P.; Németh, B. Integrated control design for driver assistance systems based on LPV methods. *Int. J. Control* **2016**, *89*, 2420–2433. [[CrossRef](#)]
18. Yoshino, T.; Nozaki, H. *Effect of Direct Yaw Moment Control Based on Steering Angle Velocity and Camber Angle Control*; SAE Technical Paper Series; SAE International: Warrendale, PA, USA, 2014.
19. Zhang, W.; Drugge, L.; Nybacka, M.; Wang, Z. Active Camber for Enhancing Path Following and Yaw Stability of Over-Actuated Autonomous Electric Vehicles. *Veh. Syst. Dyn.* **2020**, *59*, 800–821. [[CrossRef](#)]
20. REE Automotive. REE Automotive, 2022. Available online: <https://ree.auto/> (accessed on 27 January 2022).
21. Zoox. Safety, 2022. Available online: <https://zoox.com/safety/> (accessed on 27 January 2022).
22. Davari, M.M. Exploiting Over-Actuation to Reduce Tyre Energy Losses in Vehicle Manoeuvres. Ph.D. Thesis, Vehicle Dynamics, KTH Royal Institute of Technology, Stockholm, Sweden, 2017.
23. Sun, P. Improving Energy-Efficiency of Electric Vehicles by Over-Actuation. Ph.D. Thesis, Vehicle Dynamics, KTH Royal Institute of Technology, Stockholm, Sweden, 2020.
24. Rauh, J.; Ammon, D. System dynamics of electrified vehicles: Some facts, thoughts, and challenges. *Veh. Syst. Dyn.* **2011**, *49*, 1005–1020. [[CrossRef](#)]
25. Wanner, D. Controlling Over-Actuated Road Vehicles during Failure Conditions. Ph.D. Thesis, Vehicle Dynamics, KTH Royal Institute of Technology, Stockholm, Sweden, 2015.
26. Papaioannou, G.; Koulocheris, D.; Velenis, E. Skyhook control strategy for vehicle suspensions based on the distribution of the operational conditions. *Proc. Inst. Mech. Eng. Part D J. Automob. Eng.* **2021**, *235*, 2776–2790. [[CrossRef](#)]
27. Zhang, W.; Wang, Z.; Zou, C.; Drugge, L.; Nybacka, M. Advanced Vehicle State Monitoring: Evaluating Moving Horizon Estimators and Unscented Kalman Filter. *IEEE Trans. Veh. Technol.* **2019**, *68*, 5430–5442. [[CrossRef](#)]
28. Doumiati, M.; Charara, A.; Victorino, A. *Vehicle Dynamics Estimation Using Kalman Filtering: Experimental Validation*; John Wiley & Sons, Inc.: Hoboken, NJ, USA, 2012.
29. Dugoff, H.; Fancher, P.S.; Segel, L. *Tire Performance Characteristics Affecting Vehicle Response to Steering and Braking Control Inputs*; Technical Report Contract CST-460; Highway Safety Research Institute: Ann Arbor, MI, USA, 1969.
30. Rawlings, J.B.; Mayne, D.Q.; Diehl, M.M. *Model Predictive Control: Theory, Computation, and Design*, 2nd ed.; Nob Hill Publishing: Madison, WI, USA, 2017.
31. Mayne, D.; Rawlings, J.; Rao, C.; Scokaert, P. Constrained model predictive control: Stability and optimality. *Automatica* **2000**, *36*, 789–814. [[CrossRef](#)]
32. Rajamani, R. *Vehicle Dynamics and Control*, 2nd ed.; Springer: New York, NY, USA, 2012.
33. Zhang, W.; Drugge, L.; Nybacka, M.; Jerrelind, J.; Wang, Z.; Zhu, J. Exploring model complexity for trajectory planning of autonomous vehicles in critical driving scenarios. In Proceedings of the Advances in Dynamics of Vehicles on Roads and Tracks (IAVSD 2021), Saint Petersburg, Russia, 17–19 August 2021.
34. Hicks, G.A.; Ray, W.H. Approximation methods for optimal control synthesis. *Can. J. Chem. Eng.* **1971**, *49*, 522–528. [[CrossRef](#)]
35. Bock, H.G.; Plitt, K.J. A Multiple Shooting Algorithm for Direct Solution of Optimal Control Problems. In Proceedings of the Ninth Triennial World Congress of IFAC, Budapest, Hungary, 2–6 July 1984; Volume 17, pp. 1603–1608. [[CrossRef](#)]

36. Tsang, T.H.; Himmelblau, D.M.; Edgar, T.F. Optimal control via collocation and non-linear programming. *Int. J. Control* **1975**, *21*, 763–768. [[CrossRef](#)]
37. Wächter, A.; Biegler, L.T. On the implementation of an interior-point filter line-search algorithm for large-scale nonlinear programming. *Math. Program.* **2005**, *106*, 25–57. [[CrossRef](#)]
38. Robertson, D.; Lee, J. A least squares formulation for state estimation. *J. Process Control* **1995**, *5*, 291–299. [[CrossRef](#)]
39. Rao, C.; Rawlings, J.; Mayne, D. Constrained state estimation for nonlinear discrete-time systems: stability and moving horizon approximations. *IEEE Trans. Autom. Control* **2003**, *48*, 246–258. [[CrossRef](#)]
40. Zhang, W. Exploiting Over-Actuation for Improved Active Safety of Autonomous Electric Vehicles. Ph.D. Thesis, Vehicle Dynamics, KTH Royal Institute of Technology, Stockholm, Sweden, 2022.
41. Risbeck, M.J.; Rawlings, J.B. *MPCTools: Nonlinear Model Predictive Control Tools for CasADi (Python Interface)*, 2015. Available online: <https://bitbucket.org/rawlings-group/mpc-tools-casadi> (accessed on 1 June 2023).
42. Andersson, J.A.E.; Gillis, J.; Horn, G.; Rawlings, J.B.; Diehl, M. CasADi—A software framework for nonlinear optimization and optimal control. *Math. Program. Comput.* **2019**, *11*, 1–36. [[CrossRef](#)]
43. HSL. *A Collection of Fortran Codes for Large Scale Scientific Computation*; HSL: Oxford, UK, 2014.
44. Wallmark, O.; Nybacka, M.; Malmquist, D.; Burman, M.; Wennhage, P.; Georen, P. Design and Implementation of an Experimental Research and Concept Demonstration Vehicle. In Proceedings of the 2014 IEEE Vehicle Power and Propulsion Conference (VPPC), Coimbra, Portugal, 27–30 October 2014; pp. 1–6. [[CrossRef](#)]
45. Dassault Systèmes. Dymola 2017, 2016. Available online: <https://www.3ds.com/products-services/catia/products/dymola/> (accessed on 27 January 2022).
46. Pacejka, H. *Tire and Vehicle Dynamics*, 3rd ed.; Elsevier: Oxford, UK, 2012.
47. Modelica Association. *Functional Mockup Interface for Model Exchange and Co-Simulation*, Version 2.0; Modelica Association: Linköping, Sweden, 2014.
48. Xiong, L.; Xia, X.; Lu, Y.; Liu, W.; Gao, L.; Song, S.; Yu, Z. IMU-Based Automated Vehicle Body Sideslip Angle and Attitude Estimation Aided by GNSS Using Parallel Adaptive Kalman Filters. *IEEE Trans. Veh. Technol.* **2020**, *69*, 10668–10680. [[CrossRef](#)]
49. Xia, X.; Hashemi, E.; Xiong, L.; Khajepour, A.; Xu, N. Autonomous Vehicles Sideslip Angle Estimation: Single Antenna GNSS/IMU Fusion With Observability Analysis. *IEEE Internet Things J.* **2021**, *8*, 14845–14859. [[CrossRef](#)]
50. Xia, X.; Hashemi, E.; Xiong, L.; Khajepour, A. Autonomous Vehicle Kinematics and Dynamics Synthesis for Sideslip Angle Estimation Based on Consensus Kalman Filter. *IEEE Trans. Control Syst. Technol.* **2023**, *31*, 179–192. [[CrossRef](#)]

Disclaimer/Publisher’s Note: The statements, opinions and data contained in all publications are solely those of the individual author(s) and contributor(s) and not of MDPI and/or the editor(s). MDPI and/or the editor(s) disclaim responsibility for any injury to people or property resulting from any ideas, methods, instructions or products referred to in the content.